

Spontaneous polar and chiral symmetry breaking in ordered fluids - heliconical ferroelectric nematic phases

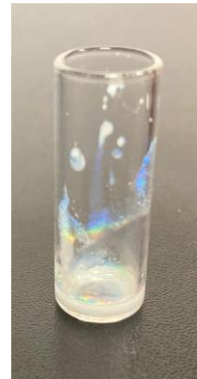
Jakub Karcz, Jakub Herman, Natan Rychłowicz and Przemysław Kula*

Faculty of Advanced Technology and Chemistry Military University of Technology

Ewa Górecka, Jadwiga Szydłowska, Paweł W. Majewski, Damian Pocięcha*

Department of Chemistry, University of Warsaw

Abstract: It is known that the chiral interaction described by Dzyaloshinskii-Moriya (DMI) term lead to the plethora of topological structures of magnetic spins, such as helical or skyrmion phases. Here we present the that analogues electrical DMI can lead to similar structural complexity of electric dipoles in soft matter. We report on a new polar liquid phase in which achiral molecules spontaneously form a heliconical structure. The helical pitch is comparable to the wavelength of visible light and unwinds critically at the transition to a uniformly polar, ferroelectric nematic phase. Although this new liquid crystalline phase resembles the twist-bend nematic phase, the mechanism of its formation is different and is attributed to electrical interactions that cause non-collinear arrangement of electric dipoles, similarly as observed for spins in magnetic systems.



Introduction: Since the discovery of ferroelectricity by Joseph Valasek in 1920 (1), the analogies and differences between electrical and magnetic systems have been discussed. Both systems show a spontaneous organization of dipole moments, but the plethora of structures exhibited by magnetic materials is much richer. In magnetic systems, in addition to simple collinear ferromagnets and antiferromagnets, a number of exotic structures have been found in which the spins twist (helical structures) or curl (skyrmions). The main reason for the emergence of such complex spin arrangements is the Dzyaloshinskii-Moriya interaction, DMI (2), which forces magnetic moments to twist. In stark contrast, the electric dipoles in solid crystals have a strong preference for collinearity and organize primarily in parallel (ferroelectric) or antiparallel (antiferroelectric) structures. The helical organization is rare (3), apparently there is no inherent mechanism for electrically polar materials that facilitates the spontaneous twisting of dipoles. The possibility of more complex polar structures induced by dipole-dipole interactions is evident in soft materials such as liquid crystals, where the energy required for elastic structural deformations is low (4). For many years, however, the idea that liquid crystals could exhibit genuine ferroelectric properties, characterized by the spontaneous ordering of electric dipole moments due to direct interactions, was considered exotic and seemingly unattainable. It was believed that the dipole interactions in liquids were too weak and the thermal fluctuations too strong to support long-range ordering of the electric dipole moments. Until recently, the ordering of dipoles in all polar liquid crystals was not directly due to dipole-dipole interactions, but resulted from steric effects (5). It was achieved by a reduction in phase symmetry driven by the chirality of molecules or by significant constraints of molecular motions resulting from the molecular shape, i.e. the bending of the molecular aromatic cores. Nevertheless, significant progress was made a few years ago with the first reports of a ferroelectric nematic phase (6-8), which immediately attracted considerable attention.

Two different types of polar nematics have been documented so far: the N_F phase, which is characterized by a uniform polar ordering with a polarization vector P aligned along the director (averaged direction of the long molecular axis) and N_x (also known as SmZ_A), which has a periodic antiferroelectric domain structure (9, 10). However, the question of whether dipole interactions can also lead to spontaneous mirror symmetry breaking and the formation of twisted structures is still open. This would be a fascinating example of chiral symmetry breaking by polar interactions, a captivating phenomenon in which an originally achiral polar or apolar system spontaneously adopts either a left-handed or right-handed polar helical configuration. The dipoles that twist could form a helical structure analogous to the nematic phase made of chiral molecules (N^* , cholesteric) in which the bulk polarization is fully compensated, or they could form a heliconical structure in which the molecules are tilted at an arbitrary angle to the helical axis with the polarization only partially compensated, a structure corresponding to the twist-bend nematic (N_{TB}) phase (11-13).

In this communication we describe the first example of ferroelectric helical phase, formed spontaneously from achiral molecules. Reported here material, 4'-(difluoro(3,4,5-trifluorophenoxy)methyl)-2,3',5'-trifluoro-[1,1'-biphenyl]-4-yl-2,6-difluoro-4-(5-propyl-1,3-dioxan-2-yl)benzoate (synthesis described in SI, Fig. S1), hereafter referred to as **MUT_JK103**, was synthesized in Liquid Crystal group of the Military University of Technology; its molecular structure is based on DIO – one of the model ferronematogens (6). The mesogenic core was elongated; in the optimized geometry (Fig. S2) the molecular length is 31.9 Å. The dipole moment, being nearly collinear with the long molecular axis (calculated angle between dipole direction and long molecular axis is 9.5°), was increased to 12.6 D by substituting additional fluorine atoms in the core. The compound **MUT_JK103** forms 5 mesophases between the solid crystal and the isotropic liquid (phase sequence given in SI). It should be emphasized that all of them are enantiotropic, with small but distinct thermal effects accompanying the phase transitions (Fig. 1).

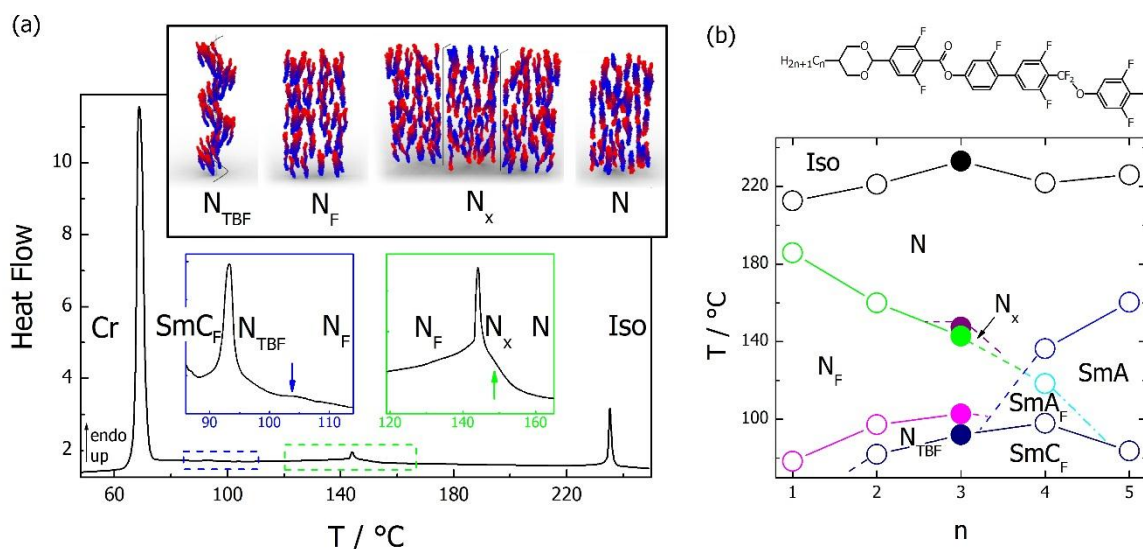


Figure 1. (a) DSC thermogram recorded on second heating scan for **MUT_JK103**, with enlarged temperature ranges of transitions between LC phases, note that all the LC phases appear above melting of solid crystal phase, Cr. In the inset schematic drawings showing molecular organization in various nematic phases, red and blue coloring of each molecule shows negative and positive ends of their dipole moments. All phases except the N phase lack a head-tail symmetry, thus polar order occurs; in N_x phase regular antiferroelectric structure of uniformly polar domains is observed, N_F phase shows global ferroelectric order, and in N_{TB} phase molecules form heliconical structure, with effective polarization along the helical axis. (b) Phase diagram for homologues series **MUT_JK10n**, general molecular structure is presented above. Filled symbols refer to homologue $n=3$, which is studied in detail. SmA_F and SmC_F refer to lamellar phases, orthogonal and tilted, respectively, with ferroelectric order.

The X-ray diffraction studies (Fig. S3) confirmed that 4 of the mesophases lack long-range positional order of molecules (the width of the diffraction signal corresponds to a positional correlation length of the order of a few molecular distances), so they are identified as nematic phases. The lowest temperature LC phase shows a one-dimensional positional order, characteristic of smectics with a liquid-like order of molecules within the smectic layer. The position of the low-angle X-ray diffraction signal in the N, N_x and N_F phases is almost independent of temperature, in the N_{TBF} phase it gradually moves to higher angles, in the smectic phase the trend continues, indicating a decrease in periodicity, possibly due to tilting of the molecules.

The phases N_F, N_{TBF} and SmC_F are polar. When a weak electric field (200 mV μm⁻¹) is applied, the planar optical texture transforms into a homeotropic, non-birefringent one as molecules realign with their dipole moments along the electric field. Moreover, they give the hysteresis loop when a triangular-wave voltage is applied (Fig. S4); the corresponding spontaneous electric polarization is of the order of 4 μC cm⁻², a typical value for other N_F materials (14). Dielectric spectroscopy revealed a strong collective relaxation mode in the kHz range (Fig. S5) in the polar nematic phases, with a static permittivity of the order of 10⁴.

Optical studies using polarized light optical microscopy (Fig. 2 and Fig. S6) showed that the highest temperature LC phase exhibits textures characteristic for the ordinary nematic phase, i.e., a uniform texture in a cell with planar anchoring, with director aligned along rubbing direction; strong flickering due to director fluctuations was observed. The transition to the lower temperature nematic phase was evidenced by the cessation of flickering and the appearance of chevron defects typical of the N_x phase with antiferroelectric structure (9). In the following N_F phase, in a cell with parallel rubbing on both surfaces, the uniform texture reappears, with optical axis along rubbing, with some parabolic defects (15) anchored to the plastic beads used as cell spacers, while in a cell with antiparallel rubbing the optically active domains in which director twists between the surfaces are observed (Fig. S7).

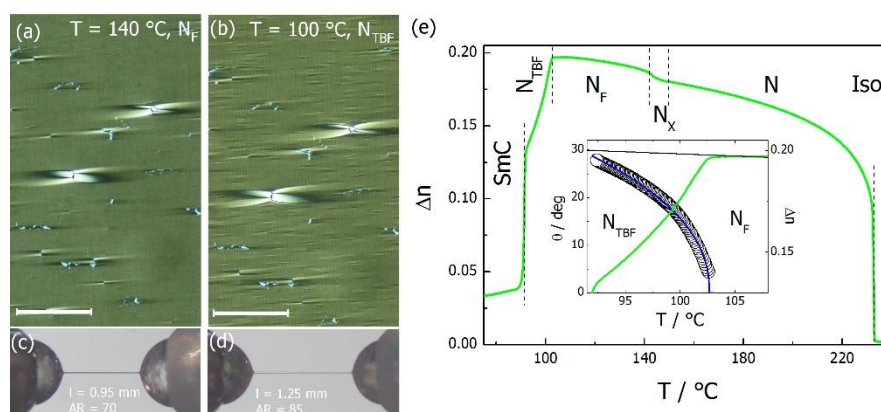


Figure 2. Optical textures observed for 1.5-μm-thick cell with parallel rubbing on both surfaces in (a) ferroelectric nematic N_F phase and (b) heliconal ferroelectric nematic phase, N_{TBF}; faint vertical stripes are oriented along the rubbing direction. Optical images were recorded between crossed polarizers (at horizontal and vertical directions), the rubbing direction was slightly inclined from vertical direction and scale bars correspond to 100 μm. Visible defects are anchored at the plastic beads used as cell spacers. Fibers drawn in (c) N_F and (d) N_{TBF} phases between two glass capillaries, images were taken just before fiber rupture. AR stands for aspect ratio of the fiber. (e) Temperature dependence of optical birefringence, Δn, measured for green light, λ=532 nm (green line); note that Δn values measured in the smectic phase are strongly affected by lack of sample alignment in this phase and resulting strong light scattering. In the inset, conical tilt angle (θ) in heliconal structure of N_{TBF} phase (circles) calculated from decrease of Δn from its extrapolated temperature dependence (black line), the blue line is a guide for the eye.

Finally, in the N_{TBF} phase, on cooling a few degrees below the phase transition, the stripes begin to form along the rubbing direction. The periodicity of the stripes depends on the cell thickness, it is 3 μm for a 1.5- μm -thick cell, for thicker cells the periodicity is larger. In the smectic phase, the texture is grainy, uncharacteristic, and strongly light-scattering.

Interestingly, the investigated material in the N_{F} and N_{TBF} phase forms easily cylindrical fibers in the form of bridges between the bulk material, these freely suspended strands between two bulky ends are of nearly constant thickness (Fig. 2cd, movie in SI). In the N_{F} phase, the fibers usually rupture when their aspect ratio (AR), i.e. length/diameter, approaches 70, which is significantly larger than predicted by Rayleigh-Plateau theory for the isotropic phase. Apparently, they are stabilized by a polar order that suppresses the fluctuation of the director (16,17). In the N_{TBF} phase, the fibers are thinner and their aspect ratio easily reaches 100 before they break, which suggests an additional mechanism that stabilizes them. Such mechanism is usually related to the internal structure of the phase, e.g. for smectic and columnar phases and is attributed to the local stiffness of the layers/columns against compression (18).

Further optical studies show that the phase transitions $N-N_x-N_{\text{F}}$ are accompanied by a slight increase in optical birefringence and thus in the orientational order of the molecules (Fig. 2). Below the $N_{\text{F}}-N_{\text{TBF}}$ phase transition, a gradual decrease in birefringence is observed, which, together with the uniform texture indicating a uniaxial structure of the phase, points to a certain averaging of the molecular positions by the formation of a heliconical structure, similar to that found in the N_{TB} phase. Assuming formation of the heliconical structure the conical tilt angle can be estimated from the decrease in birefringence (19); it develops continuously and reaches 25 degrees 10 K below the phase transition. The heliconical structure of the N_{TBF} phase also explains the additional stabilization of the fibers against rupture compared to the fibers drawn in the N_{F} phase.

Light diffraction experiments were carried out to obtain information about the pitch of the helix. In the 1.5- μm -thick cell with parallel rubbing, diffraction signals were observed in the direction perpendicular to the rubbing (Fig. 3a); their positions are nearly temperature independent and correspond to the periodicity of the stripe texture observed in microscopic studies (Fig. 2b). Moreover, additional diffraction signals were found at higher angles, which thus correspond to much lower periodicities and are aligned along the rubbing direction. A few K below the $N_{\text{F}}-N_{\text{TBF}}$ phase transition, the related periodicity is $\sim 500\text{--}600$ nm and is attributed to helical pitch length. To avoid interaction with surfaces, the diffraction experiment was also performed on thicker cells (without alignment layers) and on LC droplets deposited on glass or freely suspended LC films. In all these samples ('powder' samples), a ring pattern with nearly the same diffraction intensity across the azimuthal angle was found (Fig. 3b), which changed its position with temperature, in the range of angles corresponding to the periodicities of 550-1200 nm with increasing temperature (Fig. 3c). This proves that the helix unwinds critically when approaching the phase transition to the N_{F} phase, and the changes were reversible upon heating and cooling. Finally, by scanning the transmission of light in a micrometer-sized area, it was found that the center of the selective reflection depth shifts from 700 to 440 nm with decreasing temperature (Fig. S8). The selective reflection is blue-shifted compared to the periodicities observed in the diffraction experiment because the helices are inclined to the direction of light propagation, as indicated by a low birefringence of the sample when observed between crossed polarizers. As expected, the selective reflection is sensitive to the circular polarization of light. When small areas of a few micrometers are examined, the intensity of transmitted light decreases for only one of the circular polarizations, depending on the selected location in the sample (Fig. 3d and S8). When viewing larger areas illuminated with circularly polarized light of selected handedness, the domains that selectively reflect the light and those that do not are observed. Interestingly, the domain

boundaries remain intact even after heating the sample into the N_F phase (Fig. 3e). It can be concluded that the direction of the electric polarization in the domains is maintained during the N_{TBF} - N_F phase transition, so that the sense of the helix in the N_{TBF} phase is obviously related to the direction of the polarization.

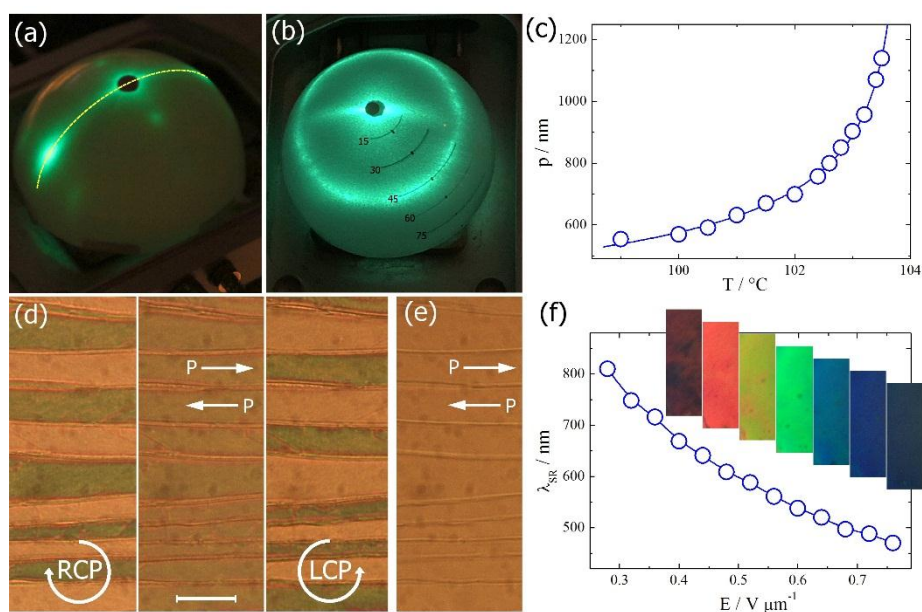


Figure 3. (a, b) Diffraction patterns recorded in the N_{TBF} phase, ~ 3 K below the N_F - N_{TBF} phase transition, sample placed on heating stage was illuminated from the bottom with a green (530 nm) laser, diffracted light was projected onto spherical screen; (a) sample prepared in 1.5- μm -thick cell with planar anchoring and parallel rubbing on both surfaces, yellow dashed line shows projection of the rubbing direction on the spherical screen, (b) sample prepared as one-free-surface droplet on untreated glass. (c) Temperature dependence of helical pitch (p) determined from diffraction experiments. (d) Images taken in N_{TBF} ($T=103$ °C), 10- μm -thick cell (with no alignment layers) was illuminated with white light (right-handed circularly polarized, unpolarized and left-handed circularly polarized for left, middle and right panels, respectively), greenish colors result from selective reflection (SR) of light, note that only one type of domains shows SR phenomenon when illuminated with circularly polarized light. Scale bar corresponds to 50 μm . (e) Image of the same sample area taken in N_F phases ($T=110$ °C). It should be noted that visible domains with opposite direction of electric polarization directions (arrows) are not affected by the N_{TBF} - N_F phase transition. (f) Changes of selective reflection wavelength, λ_{SR} , in N_{TBF} phase under application of dc electric field, E ; in the inset textures showing selective reflection colors visible for different values of applied voltage.

The microscopic observations in the N_{TBF} phase were also carried out under an electric field. The weak electric field realigned the molecules in the cell; when viewed between the crossed polarizers, the sample becomes homeotropic and splits into micrometer-sized regions with optical activity of opposite sign (Fig. S9). A further increase of electric field induces the changes in the color of the selective reflection in sequence red, green and blue. The shift in the wavelength of the selective reflection is reversible when the electric field is increased or decreased (Fig. 3f, Fig. S10). Above the critical field (~ 500 $\text{mV } \mu\text{m}^{-1}$) the optical activity disappears. Although the shortening of the helix under the electric field is surprising (the opposite effect is found in the cholesteric phase), similar changes have been reported for the twisted nematic phase made of dimers in the materials showing non-polar N_{TB} phase (20,21). Apparently, the application of an electric field shortens the helical pitch in the N_{TBF} phase, and at the same time the cone angle becomes smaller.

Second harmonic generation (SHG) experiments were performed to confirm the non-centrosymmetric structure of the polar nematic phases. A strong SHG signal is found in the N_F and N_{TBF} phases (Fig. S11),

however the signal decreases in the N_{TBF} phase compared to the N_{F} phase, which is consistent with the expected partial compensation of spontaneous polarization during the formation of the heliconical structure.

Finally, we investigated how the formation of the N_{TBF} phase is influenced by changes in the molecular structure. For this purpose, the homologue series MUT_JK10n of the mesogens was prepared, in which the terminal chain length, n , was modified, and a phase diagram was generated (Fig. 1b). The short homologues, $n = 1$ and $n = 2$, show a similar phase sequence of nematic phases as the MUT_JK103 compound, but the N_{TBF} phase becomes monotropic. For longer homologues, polar nematic phases are destabilized in favor of smectic phases, as expected for molecules with longer chains, thus stronger propensity to segregate aromatic cores and alkyl chains. However, the tendency to form polar structures remains, for $n=4$ a sequence of N, SmA (non-polar), SmA_F and SmC_F was found.

Summary and conclusion: We have observed a new type of polar nematic phase in which a sufficiently strong polar order leads to the breaking of mirror symmetry. As a result, a heliconical structure is formed spontaneously with the helical pitch in the NIR and visible light wavelength range. Although the structure is similar to the twist-bend N_{TB} phase, the mechanism of its formation is different. While the classical twist-bend nematic phase is driven by the decrease of bend elastic constant in the system caused by the specific shape of the molecule, the N_{TBF} phase is driven by polar interactions. The sign of the helix is coupled to the sign of the spontaneous electric polarization, suggesting that in the studied system the polar interactions are described by the term $P \cdot (\nabla \times P)$, analogous to the Dzyaloshinskii-Moriya term that leads to the twisting of spins in magnetic materials. The existence of an electric DMI, suggested previously for solid ferroelectrics (22), allows the generalization of ideas developed for magnetic systems and the anticipation of various DMI-related structures such as helices and skyrmions for electric soft systems that are likely to be discovered in the future.

Acknowledgments

The research was supported by the National Science Centre (Poland) under the grant no. 2021/43/B/ST5/00240 and by Military University of Technology under research project UGB 22-801. We gratefully acknowledge Polish high-performance computing infrastructure PLGrid (HPC Centers: ACK Cyfronet AGH, WCSS) for providing computer facilities and support within computational grant no. PLG/2023/016670

Authors thank to prof. N. Vaupotič for discussion and comments.

References

- [1] J. Valasek, Piezo-electric and allied phenomena in Rochelle salt. *Phys. Rev.* **17**, 475-481 (1921).
- [2] T. Moriya, Anisotropic superexchange interaction and weak ferromagnetism. *Phys. Rev.* **120**, 91-98 (1960).
- [3] D. D. Khalyavin, R. D. Johnson, F. Orlandi, P. G. Radaelli, A. Belik, Emergent helical texture of electric dipoles. *Science* **369**, 680-684, (2020).
- [4] A. G. Khachatryan, Development of Helical Cholesteric Structure in a Nematic Liquid-Crystal Due to Dipole-Dipole Interaction. *J. Phys. Chem. Solids* **36**, 1055-1061 (1975).

- [5] H. Takezoe, E. Gorecka, M. Čepič, Antiferroelectric liquid crystals: Interplay of simplicity and complexity. *Rev. Mod. Phys.* **82**, 897-937 (2010).
- [6] H. Nishikawa, K. Shiroshita, H. Higuchi, Y. Okumura, Y. Haseba, S. I. Yamamoto, K. Sago, H. Kikuchi, A Fluid Liquid-Crystal Material with Highly Polar Order. *Adv Mater* **29**, 1702354 (2017).
- [7] R. J. Mandle, S. J. Cowling, J. W. Goodby, A nematic to nematic transformation exhibited by a rod-like liquid crystal. *Phys. Chem. Chem. Phys.* **19**, 11429-11435 (2017).
- [8] A. Mertelj, L. Cmok, N. Sebastián, R. J. Mandle, R. R. Parker, A. C. Whitwood, J. W. Goodby, M. Čopič, Splay Nematic Phase. *Phys Rev X* **8**, 041025 (2018).
- [9] X. Chen, V. Martinez, E. Korblova, G. Freychet, M. Zhernenkov, M. A. Glaser, C. Wang, C. Zhu, L. Radzihovsky, J. E. Maclennan, D. M. Walba, N. A. Clark, The smectic ZA phase: Antiferroelectric smectic order as a prelude to the ferroelectric nematic. *Proc. Natl. Acad. Sci. USA*, **120**, e2217150120 (2022).
- [10] E. Cruickshank, P. Rybak, M. M. Majewska, S. Ramsay, C. Wang, C. Zhu, R. Walker, J. M. D. Storey, C. T. Imrie, E. Górecka, D. Pocięcha, To Be or Not To Be Polar: The Ferroelectric and Antiferroelectric Nematic Phases. *ACS Omega* **8**, 36562-36568 (2023).
- [11] M. Cestari, S. Diez-Berart, D. A. Dunmur, A. Ferrarini, M. R. de la Fuente, D. J. B Jackson, D. O. Lopez, G. R. Luckhurst, M. A. Perez-Jubindo, R. M. Richardson, J. Salud, B. A. Timimi, H. Zimmermann, Phase behavior and properties of the liquid-crystal dimer 1",7"-bis(4-cyanobiphenyl-4'-yl) heptane: A twist-bend nematic liquid crystal. *Phys Rev E* **84**, 031704 (2011)
- [12] V. Borshch, Y. K. Kim, J. Xiang, M. Gao, A. Jakli, V. P. Panov, J. K. Vij, C. T. Imrie, M. G. Tamba, G. H. Mehl, O. D. Lavrentovich, Nematic twist-bend phase with nanoscale modulation of molecular orientation. *Nature Commun.* **4**, 2635 (2013).
- [13] D. Chen, J. H. Porada, J. B. Hooper, A. Klitnick, Y. Shen, M. R. Tuchband, E. Korblova, D. Bedrov, D. M. Walba, M. A. Glaser, J. E. Maclennan, N. A. Clark, Chiral heliconical ground state of nanoscale pitch in a nematic liquid crystal of achiral molecular dimers. *Proc. Natl. Acad. Sci. USA* **110**, 15931-6 (2013).
- [14] R. Saha, P. Nepal, C. Feng, M. S. Hossain, M. Fukuto, R. Li, J. T. Gleeson, S. Sprunt, R. J. Twieg, A. Jáklí, Multiple ferroelectric nematic phases of a highly polar liquid crystal compound, *Liq. Cryst.* **49**, 1784-1796 (2022).
- [15] P. Kumari, B. Basnet, H. Wang, O. D. Lavrentovich, Ferroelectric nematic liquids with conics. *Nat Commun.* **14**, 748 (2023).
- [16] A. Jarosik, H. Nádasi, M. Schwidder, A. Manabe, M. Bremer, M. Klasen-Memmer, A. Eremin, Fluid fibres in true 3D ferroelectric liquids. arXiv:2307.12412 [cond-mat.soft] (2023)
- [17] M. T. Máthé, K. Perera, Á. Buka, P. Salamon, A. Jáklí, Fluid ferroelectric filaments, arXiv:2307.16588 [cond-mat.soft] (2023).
- [18] D. H. Van Winkle, N. A. Clark, Freely Suspended Strands of Tilted Columnar Liquid Crystal Phases: One-Dimensional Nematics with Orientational Jumps. *Phys. Rev. Lett.* **48**, 1407-1411 (1982)
- [19] C. Meyer, G. R. Luckhurst, I. Dozov, The temperature dependence of the heliconical tilt angle in the twist-bend nematic phase of the odd dimer CB7CB. *J. Mater. Chem. C* **3**, 318-328, (2015).
- [20] J. Xiang, Y. Li, Q. Li, D. A. Paterson, J. M. Storey, C. T. Imrie, O. D. Lavrentovich, Electrically tunable selective reflection of light from ultraviolet to visible and infrared by heliconical cholesterics. *Adv. Mater.* **27**, 3014-8 (2015)

- [21] C. Yuan, W. Huang, Z. Zheng, B. Liu, H. K. Bisoyi, Y. Li, D. Shen, Y. Lu, Q. Li, Stimulated Transformation of Soft Helix among Helicoidal, Heliconical and Their Inverse Helices. *Sci. Adv.* **5**, aax9501 (2019).
- [22] H. J. Zhao, P. Chen, S. Prosandeev, S. Artyukhin, L. Bellaiche, Dzyaloshinskii–Moriya-like interaction in ferroelectrics and antiferroelectrics. *Nat. Mater.* **20**, 341–345 (2021).
- [23] Gaussian 16, Revision C.01, M. J. Frisch, G. W. Trucks, H. B. Schlegel, G. E. Scuseria, M. A. Robb, J. R. Cheeseman, G. Scalmani, V. Barone, G. A. Petersson, H. Nakatsuji, X. Li, M. Caricato, A. V. Marenich, J. Bloino, B. G. Janesko, R. Gomperts, B. Mennucci, H. P. Hratchian, J. V. Ortiz, A. F. Izmaylov, J. L. Sonnenberg, D. Williams-Young, F. Ding, F. Lipparini, F. Egidi, J. Goings, B. Peng, A. Petrone, T. Henderson, D. Ranasinghe, V. G. Zakrzewski, J. Gao, N. Rega, G. Zheng, W. Liang, M. Hada, M. Ehara, K. Toyota, R. Fukuda, J. Hasegawa, M. Ishida, T. Nakajima, Y. Honda, O. Kitao, H. Nakai, T. Vreven, K. Throssell, J. A. Montgomery, Jr., J. E. Peralta, F. Ogliaro, M. J. Bearpark, J. J. Heyd, E. N. Brothers, K. N. Kudin, V. N. Staroverov, T. A. Keith, R. Kobayashi, J. Normand, K. Raghavachari, A. P. Rendell, J. C. Burant, S. S. Iyengar, J. Tomasi, M. Cossi, J. M. Millam, M. Klene, C. Adamo, R. Cammi, J. W. Ochterski, R. L. Martin, K. Morokuma, O. Farkas, J. B. Foresman, and D. J. Fox, Gaussian, Inc., Wallingford CT, 2016.
- [24] A. D. Becke, Density-functional thermochemistry. III. The role of exact exchange. *J. Chem. Phys.* **98**, 5648–5652 (1993).
- [25] C. Lee, W. Yang, R. G. Parr, Development of the Colle-Salvetti correlation-energy formula into a functional of the electron density. *Phys. Rev.* **37**, 785–789 (1988).
- [26] S. Grimme, J. Antony, S. Ehrlich, H. Krieg, A consistent and accurate ab initio parametrization of density functional dispersion correction (DFT-D) for the 94 elements H-Pu. *J. Chem. Phys.* **132** (2010).
- [27] E. Papajak, J. Zheng, X. Xu, H. R. Leverentz, D. G. Truhlar, Perspectives on basis sets beautiful: seasonal plantings of diffuse basis functions. *J. Chem. Theory Comput.* **7**, 3027–3034 (2011).
- [28] C. F. Macrae, I. Sovago, S. J. Cottrell, P. T. A. Galek, P. McCabe, E. Pidcock, M. Platings, G. P. Shields, J. S. Stevens, M. Towler and P. A. Wood, Mercury 4.0: from visualization to analysis, design and prediction. *J. Appl. Cryst.* **53**, 226-235, 2020
- [29] L. Tian, F. Chen, Multiwfn: A multifunctional wavefunction analyzer. *J. Comp. Chem.* **33**, 580–592 (2011).
- [30] J. Karcz, N. Rychłowicz, M. Czarnecka, A. Kocot, J. Herman, P. Kula, Enantiotropic ferroelectric nematic phase in a single compound. *Chem. Comm.* doi: 10.1039/d3cc04296k (2023).

Spontaneous polar and chiral symmetry breaking in ordered fluids - heliconical ferroelectric nematic phases

Jakub Karcz, Jakub Herman, Natan Rychłowicz and Przemysław Kula*

Faculty of Advanced Technology and Chemistry Military University of Technology

Ewa Górecka, Jadwiga Szydłowska, Paweł W. Majewski, Damian Pocięcha*

Department of Chemistry, University of Warsaw

Experimental methods:

For *differential scanning calorimetry* (DSC) studies, a TA Q200 calorimeter was used, calibrated using indium and zinc standards. Heating and cooling rates were 5-20 K min⁻¹, samples were kept in nitrogen atmosphere. The transition temperatures and associated thermal effects were extracted from the heating traces.

X-ray diffraction (XRD) studies in broad angle range were performed with Bruker GADDS system (micro-focus type X-ray tube with Cu anode, Vantec 2000 area detector) equipped with modified Linkam heating stage. Sample was prepared in form of small drop placed on a heated surface. For small angle diffraction experiments Bruker Nanostar system was used (micro-focus type X-ray tube with Cu anode, MRI TCPU-H heating stage, Vantec 2000 area detector). Sample was prepared in thin-walled glass capillary.

Optical studies were performed using a Zeiss Axio Imager A2m polarized light microscope, equipped with a Linkam TMS 92 heating stage. Samples were prepared in commercial cells (AWAT) of various thicknesses (1.5–20 μm) with ITO electrodes and surfactant layers for planar/homeotropic alignment.

Optical birefringence was measured with a setup consisting of a photoelastic modulator (PEM-90, Hinds) working at the base frequency $f=50$ kHz, a halogen lamp (Hamamatsu LC8) equipped with a narrow bandpass filter (532±3 nm) as a light source. The intensity of the transmitted light was measured with a photodiode (FLC Electronics PIN-20) and de-convoluted with a lock-in amplifier (EG&G 7265) into $1f$ and $2f$ components to yield a retardation induced by the sample. Glass cells with a thickness of 1.5 μm and surfactant assuring planar anchoring condition were used. Basing on measured optical birefringence the conical tilt angle (θ) in the twist-bend ferroelectric nematic phase (N_{TBF}) was deduced from the decrease of the Δn with respect to the values measured in the nematic (N_F) phase, according to relation: $\Delta n_{N_{TBF}} = \Delta n_{N_F}(3 \cos^2 \theta - 1)/2$ (19). The birefringence of the ferroelectric nematic phase was extrapolated to the lower temperature range by assuming a power law temperature dependence: $\Delta n_{N_F} = \Delta n_0(T_c - T)^\gamma$, where Δn_0 , T_c , and γ are the fitting parameters.

Optical diffraction studies were performed for the samples placed on heating stage and illuminated with green (520 nm) laser light. The diffraction pattern was recorded on the half-sphere screen placed above the sample.

Selective light reflection studies were carried out for material placed in the glass cell with ITO electrodes, either having surfactant layer assuring planar anchoring prior application of electric field or without alignment layers. Light transmission/reflection was monitored with fiber spectrometer (Filmetrics F20-UV) mounted to the Zeiss Axio Imager A2m microscope.

Fibers drawing: The fibers were drawn between two capillaries, immersed before experiment in the LC material to provide large material reservoir. To ensure the temperature control the capillaries were placed in small box having glass walls with transparent ITO heaters. The aspect ratio at which the fiber rupture occurred were obtained by analyzing the movie showing the process of fiber thinning.

Electric polarization measurements were performed using cells with ITO electrodes and no surfactant layers. The spontaneous polarization was calculated by analyzing the voltage changes on a capacitor connected in series with the cell under test, upon application of triangular-wave voltage. Siglent SDG2042X arbitrary waveform generator, FLC A200 amplifier and Siglent SDS2000X Plus oscilloscope were used.

Dielectric spectroscopy: The complex dielectric permittivity was measured in the 1 Hz–10 MHz frequency range using a Solartron 1260 impedance analyzer. The material was placed in 3- μm -thick glass cell with ITO electrodes (and no polymer alignment layer to avoid the influence of the high capacitance of a thin polymer layer).

Second Harmonic Generation: The SHG response was investigated using a setup based on a solid-state IR laser EKSPLA NL202, $\lambda=1064$ nm. The 9 ns laser pulses at a 10 Hz repetition rate and ~ 2 mJ max pulse energy were applied. The pulse energy was adjusted to avoid material decomposition. The infra-red beam was incident onto a LC cell of thickness 10 μm . An IR pass filter was placed at the entrance to the sample and a green pass filter at the exit of the sample. The emitted SHG radiation was detected using a photon counting head (Hamamatsu H7421) with a power supply unit (C8137). The signal intensity was estimated by a custom-written Python script reading the oscilloscope output signal (Agilent Technologies DSO6034A).

Molecular Modeling: The geometric parameters were calculated with quantum mechanical calculations using Gaussian 16 (Revision C.01) software package (23) on the PLGrid ASK Cyfronet Ares cluster. Geometry of the molecule was calculated with B3LYP (24,25) hybrid DFT functional with Grimme's D3 dispersion correction (26) and may-cc-pVTZ basis set(27). Frequency calculations were performed to confirm that the obtained geometry corresponds to the true minimum. Single point calculation on the same level of theory was performed to obtain the dipole moment. Output files were rendered using Mercury(28). The size of the molecule was determined using the Multiwfn software (29) – molecule was rotated to make its principal axes parallel to the three Cartesian axes and boundary atoms were determined. For the new coordinate system, angle between the direction of the dipole moment and molecular axis(X axis) was calculated.

Nuclear Magnetic Resonance: the proton (^1H), carbon (^{13}C), and fluorine (^{19}F) NMR spectra in CDCl_3 or $\text{DMSO}-d_6$ were collected using a Bruker, model Avance III spectrometer (Bruker, Billerica, MA, USA).

Organic synthesis:

Molecular structure of the studied here material, 4'-(difluoro(3,4,5-trifluorophenoxy)methyl)-2,3,5'-trifluoro-[1,1'-biphenyl]-4-yl 2,6-difluoro-4-(5-propyl-1,3-dioxan-2-yl)benzoate, referred to later as MUT_JK103, synthesized at Liquid Crystal group of the Military University of Technology is based on DIO – one of the model ferronematogens [6]. The synthetic route was divided into two parts (Fig. S1); in the first part, 3,5-difluorobenzaldehyde (**2**) was synthesized by formylation of previously obtained Grignard reagent. Next, the 1,3-dioxane ring was introduced into the molecule (**3**), which was later lithiated and carboxylated producing corresponding carboxylic acid (**4**). In the second part, in the Suzuki-Miyaura reaction the phenol (**7**) was obtained by reacting boronic ester (**6**), obtained previously from bromo derivative (**5**) in a Miyaura borylation reaction, with the 4-bromo-3-fluorophenol. Finally, **MUT_JK103** compound was synthesized in a Steglich esterification reaction between (**4**) and (**7**) with the presence of DCC and DMAP. The final compound was purified using recrystallization technique. The synthesis of (**2**), (**3**), (**4**) and (**6**) has been described previously [30] The other homologs of **MUT_JK10n** series were synthesized using analogues methods.

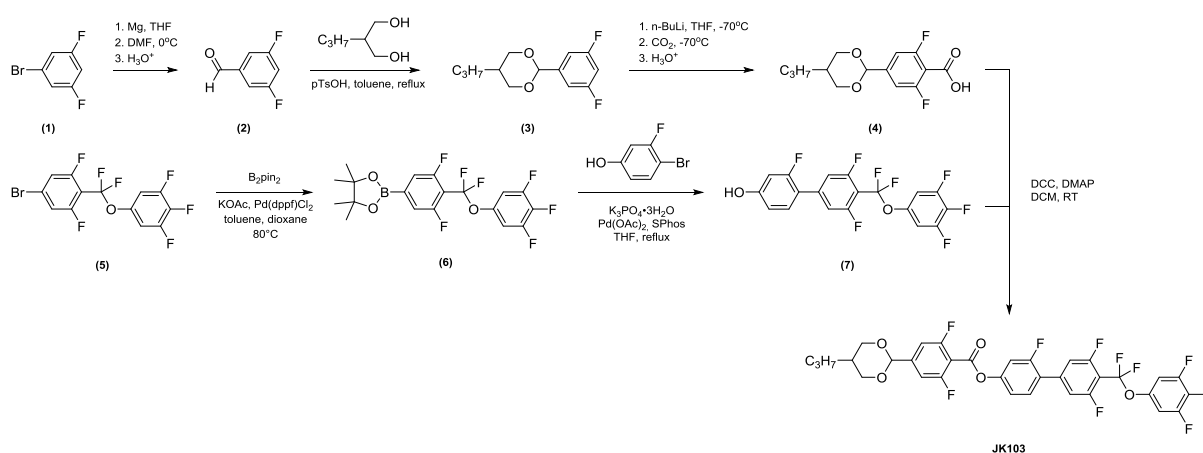


Figure S1. Synthesis of studied compound MUT_JK103

4'-(difluoro(3,4,5-trifluorophenoxy)methyl)-2,3,5'-trifluoro-[1,1'-biphenyl]-4-ol (**7**)

The mixture of 2-(4-(difluoro(3,4,5-trifluorophenoxy)methyl)-3,5-difluorophenyl)-4,4,5,5-tetramethyl-1,3,2-dioxaborolane (**6**) (5.71 g; 0.0131 mol), 4-bromo-3-fluorophenol (2.27 g; 0.0119 mol), potassium phosphate trihydrate (11.11 g; 0.0417 mol) in anhydrous THF (100 ml) was refluxed for 1h under N₂ atmosphere. Then Pd(OAc)₂ and SPhos was added and mixture was stirred at reflux for 2h. Later, it was cooled down, acidified using 10% HCl solution and extracted with DCM. The organic layer was then dried over MgSO₄, concentrated under vacuum. The residue was recrystallized from hexane to give off-white solid.

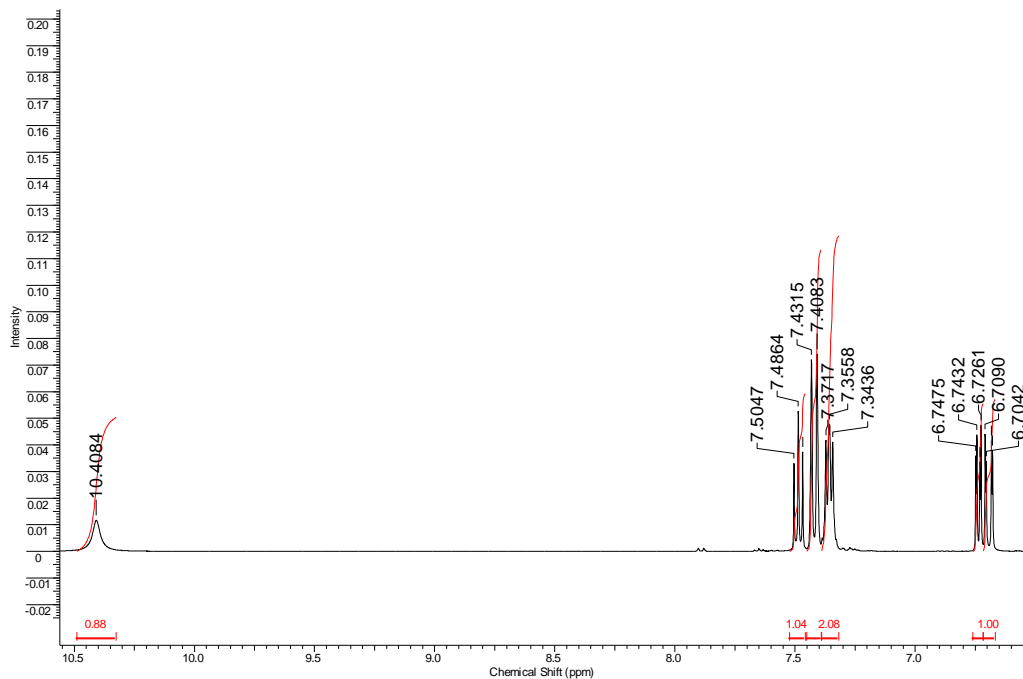
Yield 4.27g (85.4%)

Purity 96.9% (GC-MS)

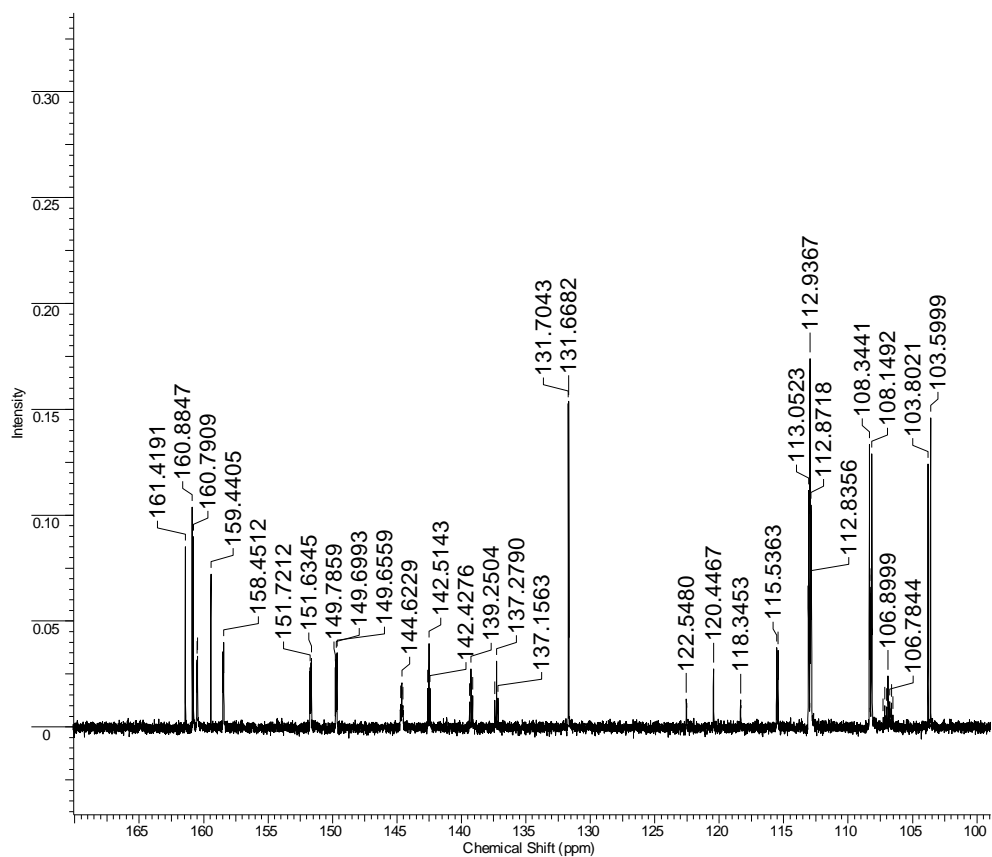
m.p. = 79°C

MS(EI) m/z: 420 (M+); 401; 273; 244; 224; 204; 175; 156; 136; 119

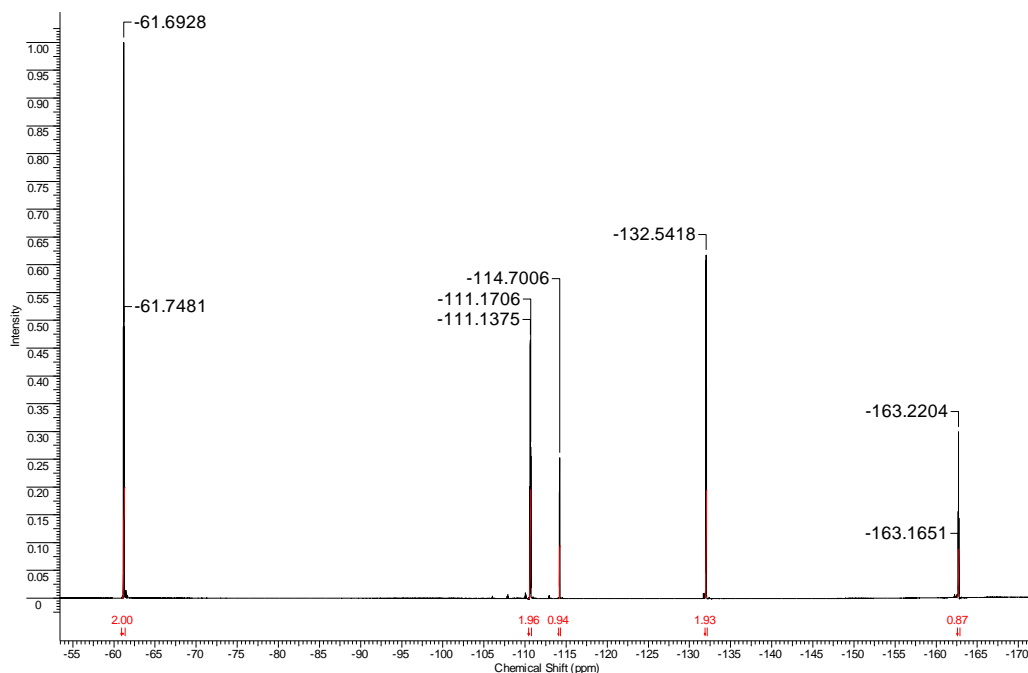
^1H NMR (500 MHz, DMSO- d_6) δ : 10.41 (s, 1H, Ar-OH); 7.49 (t, $J=9.15$ Hz, 1H, Ar-H); 7.42 (d, $J=11.60$ Hz, 2H, Ar-H); 7.36 (dd, $J=7.93, 6.10$ Hz, 2H, Ar-H); 6.74 (dd, $J=8.55, 2.14$ Hz, 1H, Ar-H); 6.69 (dd, $J=13.12, 2.44$ Hz, 1H, Ar-H)



^{13}C NMR (125 MHz, DMSO- d_6) δ : 161.42; 160.84 (d, $J=11.81$ Hz); 160.50 (d, $J=6.36$ Hz); 159.44; 158.48 (d, $J=6.36$ Hz); 150.71 (dq, $J=248.76, 5.34, 5.22, 5.00$ Hz); 144.63 (m); 142.52 (t, $J=11.35$ Hz); 138.26 (dt, $J=247.96, 15.44$ Hz); 131.69 (d, $J=4.54$ Hz); 120.45 (t, $J=264.31$ Hz); 115.49 (d, $J=11.81$ Hz); 112.96 (m); 108.25 (m); 106.90 (m); 103.70 (d, $J=25.43$ Hz)



^{19}F NMR (471 MHz, CDCl_3) δ : -61.69 (t, $J=26.0$ Hz, 2F); -111.13 (td, $J=26.0, 10.4$ Hz, 2F); -114.70 (t, $J=10.4$ Hz, 1F); -132.53 (dd, $J=20.8, 8.7$ Hz, 2F); -163.22 (tt, $J=20.8, 5.2$ Hz, 1F)



4'-(difluoro(3,4,5-trifluorophenoxy)methyl)-2,3',5'-trifluoro-[1,1'-biphenyl]-4-yl 2,6-difluoro-4-(5-propyl-1,3-dioxan-2-yl)benzoate (MUT_JK103)

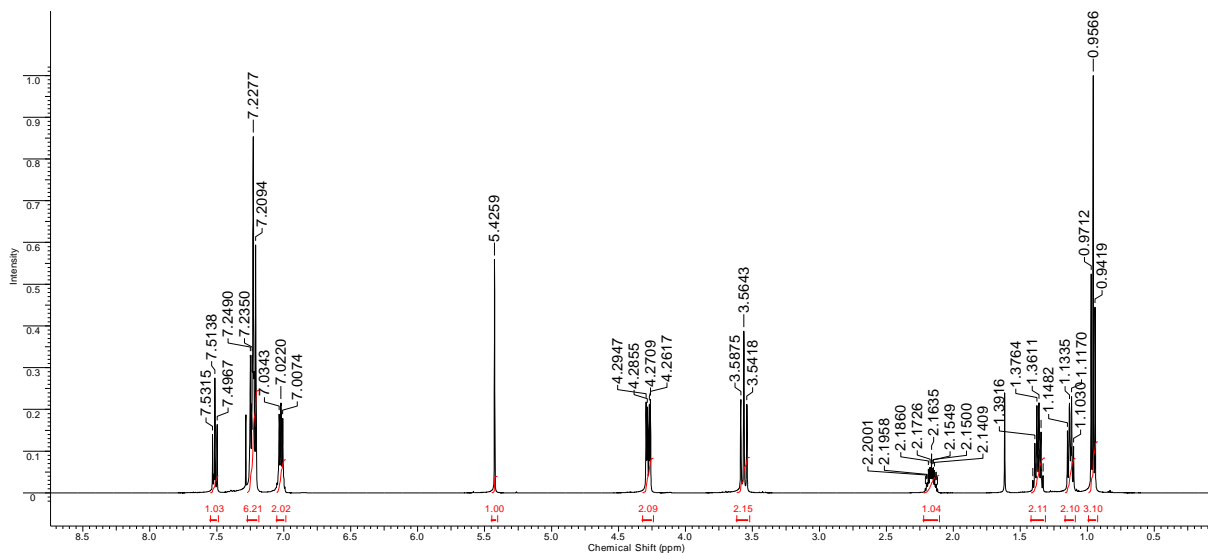
To a stirred solution of 2,6-difluoro-4-(5-propyl-1,3-dioxan-2-yl)benzoic acid (**4**) (1.24 g; 0.00433 mol), 4'-(difluoro(3,4,5-trifluorophenoxy)methyl)-2,3',5'-trifluoro-[1,1'-biphenyl]-4-ol (**7**) (2 g; 0.00476 mol) and DCC (0.98 g; 0.00476 mol) DMAP (0.1g) was added and the solution was stirred overnight at room temperature. The reaction mixture was filtered through silica pad and the filtrate was concentrated under vacuum. The residue was then recrystallized from ethanol/acetone mixture to give white solid.

Yield 2.1g (70.5%)

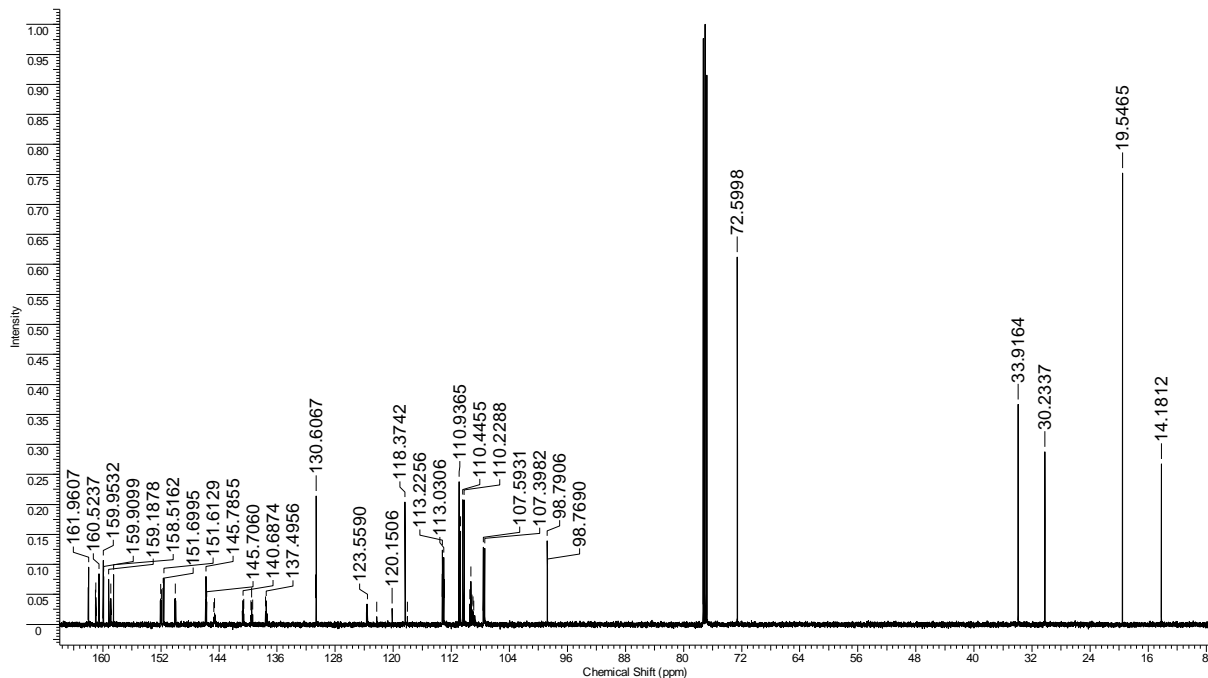
Purity 99.6% (LC-MS)

MS(EI) m/z : 687 (M⁺); 669; 590; 569; 541; 441; 419; 384; 269; 244; 220; 193; 169; 141s

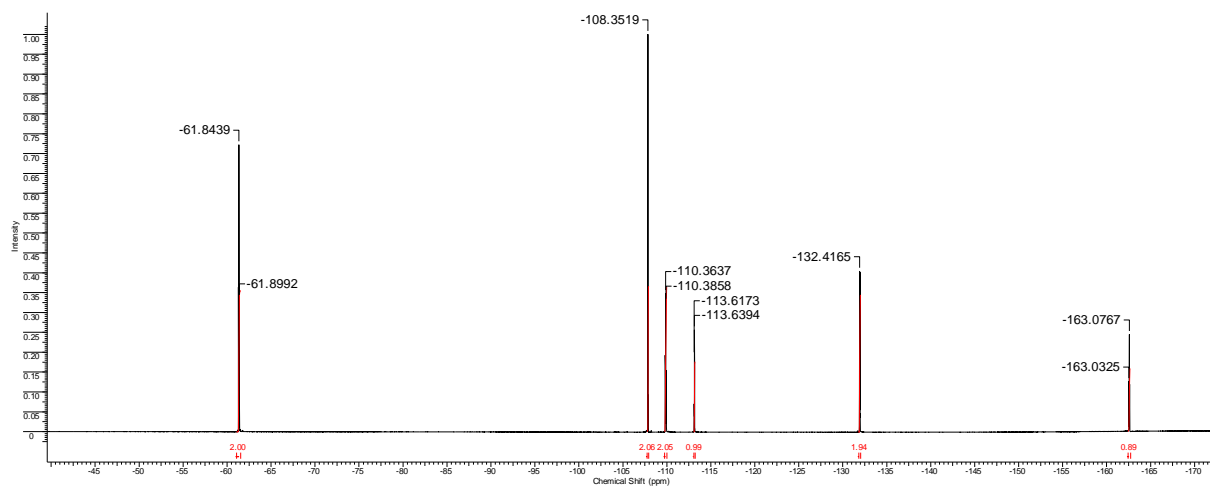
^1H NMR (500 MHz, CDCl_3) δ : 7.51 (t, $J=8.70$ Hz, 1 H); 7.23 (m, 6 H); 7.02 (dd, $J=7.32, 6.10$ Hz, 2 H); 5.43 (s, 1 H); 4.28 (dd, $J=11.90, 4.58$ Hz, 2 H); 3.56 (t, $J=11.44$ Hz, 2 H); 2.16 (m, 1 H); 1.37 (m, 2 H); 1.12 (m, 2 H); 0.96 (t, $J=7.32$ Hz, 3 H)



^{13}C NMR (125 MHz, CDCl_3) δ : 161.98 (d, $J=5.45$ Hz); 160.98 (d, $J=6.36$ Hz); 160.52; 159.93 (d, $J=5.45$ Hz); 159.19; 158.93 (d, $J=6.36$ Hz); 158.52; 152.02 (q, $J=10.90$, 5.45 Hz); 151.66 (d, $J=10.90$ Hz); 150.03 (q, $J=10.90$, 5.45 Hz); 145.79 (t, $J=9.99$ Hz); 144.62 (m); 140.69 (t, $J=10.90$ Hz); 138.49 (dt, $J=250.69$, 15.44 Hz); 130.62 (d, $J=3.63$ Hz); 123.61 (d, $J=12.72$ Hz); 120.15 (t, $J=266.13$ Hz); 118.36 (d, $J=3.63$ Hz); 113.13 (dd, $J=27.70$, 3.18 Hz); 110.94; 110.73; 110.33 (m); 109.09 (m); 107.50 (m); 98.79 (t, $J=2.27$ Hz); 72.60; 33.92; 30.23; 19.55; 14.18



^{19}F NMR (471 MHz, CDCl_3) δ : -61.84 (t, $J=26.0$ Hz, 2F); -108.36 (d, $J=8.7$ Hz, 2F); -110.37 (td, $J=26.0$, 10.4 Hz, 2F); -113.64 (t, $J=10.4$ Hz, 1F); -132.43 (dd, $J=20.8$, 7.0 Hz, 2F); -163.08 (tt, $J=20.8$, 5.2 Hz, 1F)



Additional results:

Phase sequence, phase transition temperatures (in °C) and associated thermal effects (in parentheses, kJ mol^{-1}) for compound **MUT_JK103**, obtained from DSC studies, values were extracted from second heating scan.

Cr 67.4 (20.24) SmC_F 90.9 (0.06) N_{TBF} 103.3 (0.0007) N_F 143.1 (0.28) N_X 150.7 (0.02^a) N 234.1 (1.10) Iso

^a heat capacity jump, in $\text{kJ mol}^{-1} \text{K}^{-1}$

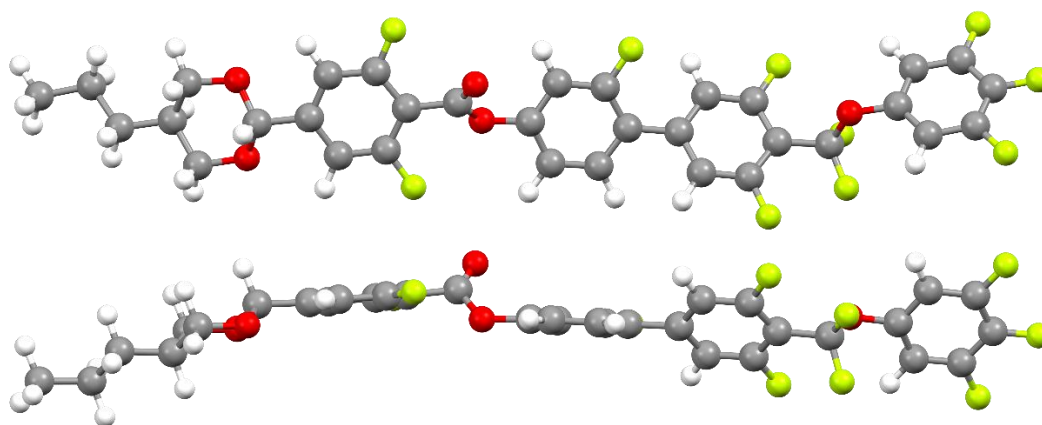


Figure S2. Optimized molecular structure of MUT_JK103.

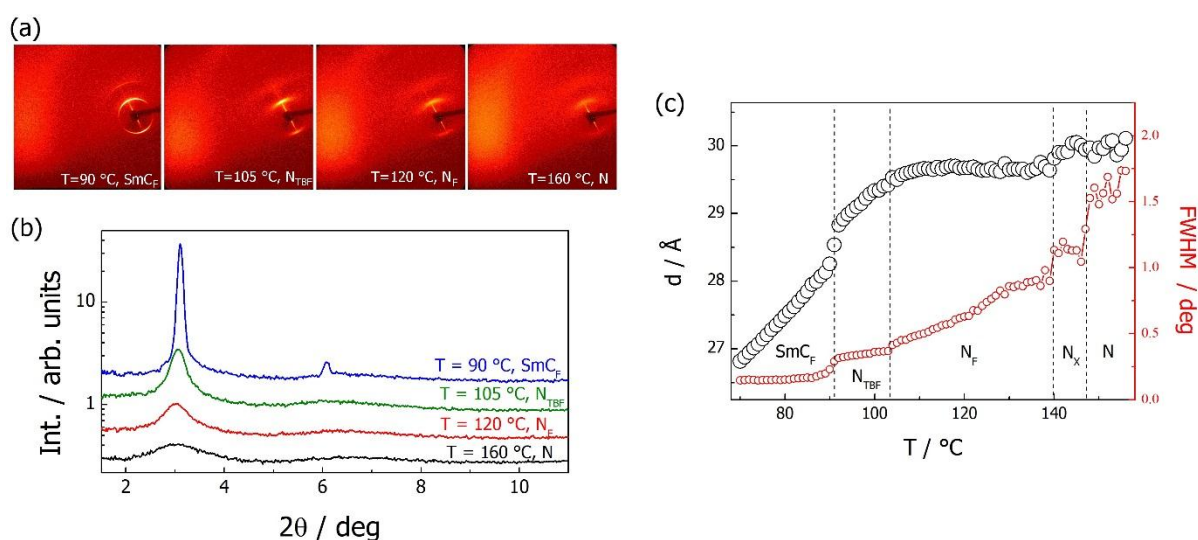


Figure S3. (a) Broad-angle 2D XRD patterns taken for partially aligned sample of MUT_JK103 in the SmC_F, N_{TBF}, N_F and N phases, at the indicated temperatures. (b) X-ray diffractograms obtained by integration of 2D patterns given in (a), curves were vertically shifted for clarity of presentation, diffracted intensity is given in logarithmic scale. (c) Layer spacing in smectic phase and local periodicity of the structure in nematic phases (black circles) measured vs. temperature by small-angle XRD. Full width at half maximum (FWHM, red circles) of the diffraction signal evidences growth of the correlation length of positional order on approaching smectic phase, in the smectic phase the positional order becomes long-range, the higher temperature phases are identified as nematic phases.

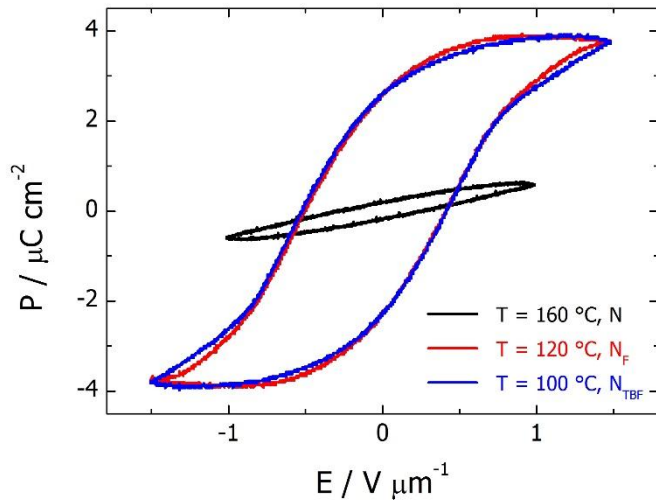


Figure S4. Hysteresis loops for electric polarization switching recorded in the N, N_F and N_{TBF} phases under application of triangular-wave voltage of frequency 30 Hz. Saturated values of polarization in the N_F and N_{TBF} phases, $\sim 4 \mu\text{C cm}^{-2}$, are typical for ferromagnetic materials.

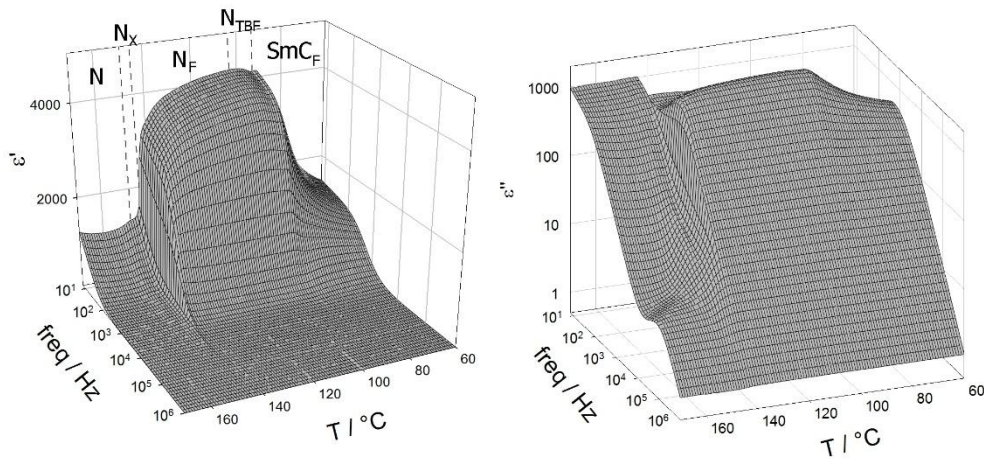


Figure S5. Real (ϵ') and imaginary (ϵ'') parts of permittivity recorded for compound MUT_JK103 in 3- μm -thick cell with bare ITO electrodes (without aligning polymer layers). Only small changes are visible at N_F - N_{TBF} phase transitions, apparently both phases are ferroelectric, with very similar polar properties.

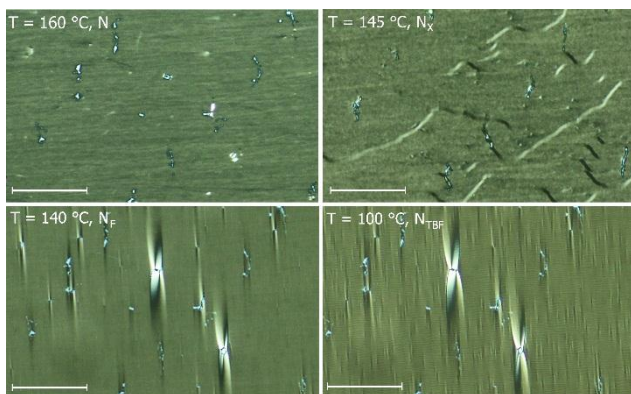


Figure S6. Optical textures observed in four nematic phases (N , N_x , N_F and N_{TBF}) of compound MUT_JK103. Sample was prepared in 1.5- μm -thick cell with planar anchoring and parallel rubbing on both surfaces. Images were recorded between crossed polarizers (at horizontal and vertical directions), rubbing direction was slightly inclined from vertical direction and scale bars correspond to 100 μm . Chevron defects visible in upper right panel allowed for identification of N_x phase.

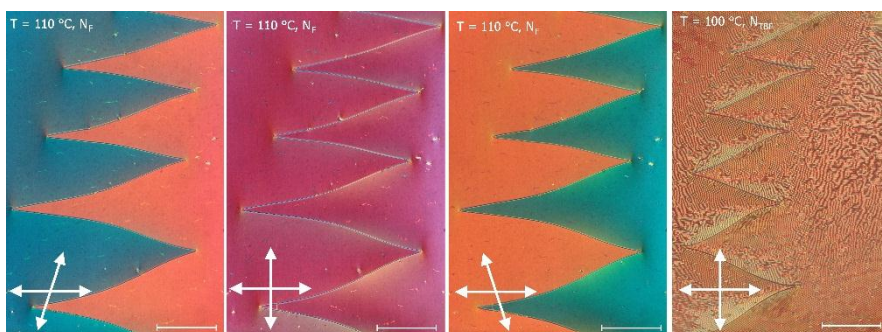


Figure S7. Optical textures observed in the N_F and N_{TBF} phases of compound MUT_JK103. Sample was prepared in 5- μm -thick cell with planar anchoring and antiparallel rubbing on both surfaces. Images were recorded either between crossed polarizers or after slight de-crossing of polarizers in opposite directions (polarizers orientation marked by arrows). Visible optical activity is due to twisted (TN) states induced by antiparallel orientation of molecules at both surfaces. Scale bars correspond to 200 μm .

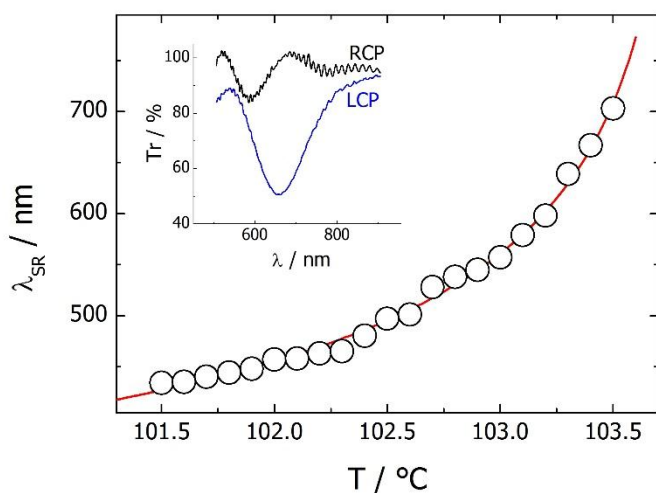


Figure S8. Selective reflection wavelength (λ_{SR}) measured vs. temperature by scanning the transmission of light in micron-sized sample area, the selective reflection is blue shifted comparing to helical pitch length determined in light diffraction experiments – apparently the helices are inclined to the light propagation direction. Selective reflection was found sensitive to the handedness of circular polarization of light, the transmitted light intensity shows a deep only for one of the circular polarizations (see inset), depending on the place in the sample.

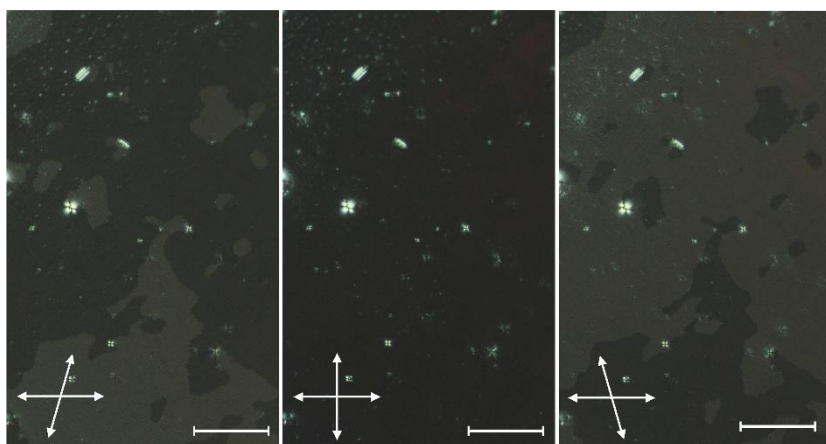


Figure S9. Non-birefringent texture of N_{TBF} phase ($T = 97\text{ }^{\circ}\text{C}$) with optically active domains (clearly visible by de-crossing of polarizers, arrows), recorded in $5\text{-}\mu\text{m}$ -thick cell with planar anchoring under application of weak dc electric field, $0.25\text{ V }\mu\text{m}^{-1}$. Electric field causes realignment of the sample - the helix becomes oriented along light propagation direction. The domains of opposite optical activity correspond to areas in which the helix has opposite handedness. Scale bars correspond to $100\text{ }\mu\text{m}$.

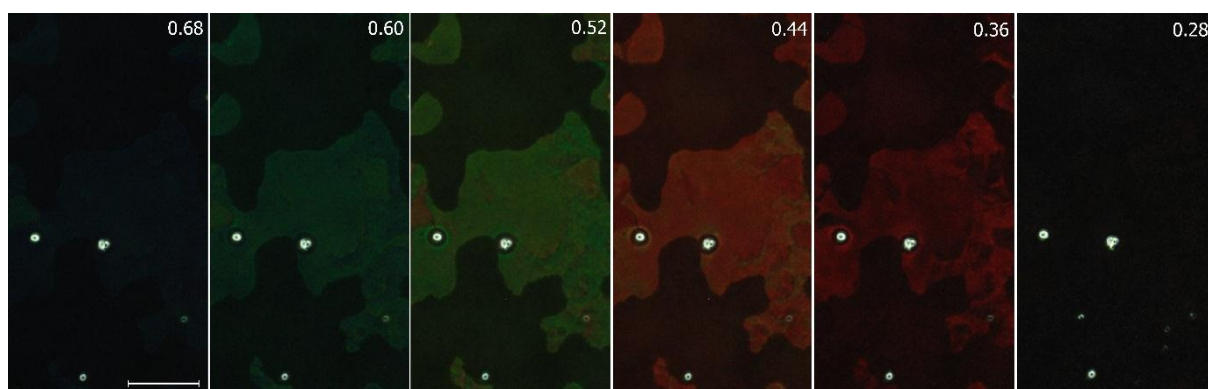


Figure S10. Microscopic images presenting selective reflection of light in N_{TBF} phase ($T = 97\text{ }^{\circ}\text{C}$), they were taken for $5\text{-}\mu\text{m}$ -thick cell with no alignment layers under application of dc electric field (indicated in upper right corners, in $\text{V }\mu\text{m}^{-1}$). Two types of domains are visible, showing opposite signs of optical activity due to opposite handedness of the helix, one type of the domains is brought into light extinction condition by slightly de-crossing polarizers. Wavelength of reflection band strongly changes through whole visible range with applied electric field – apparently helical pitch gets shorter with increasing of applied voltage. Scale bar corresponds to $100\text{ }\mu\text{m}$.

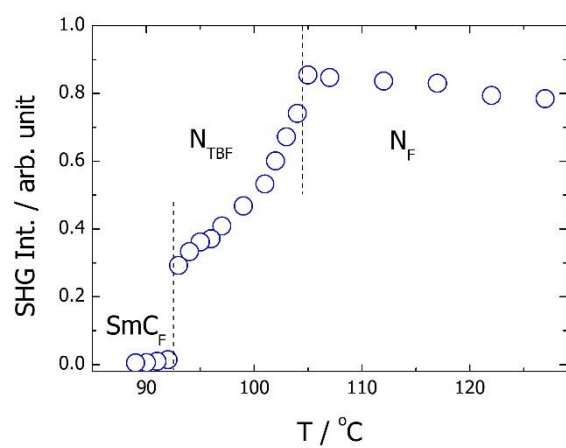


Figure S11. Intensity of SHG signal (in arbitrary units) measured vs. temperature for compound MUT_JK103. Decrease of SHG in N_{TBF} phase relative to N_F phase is related to partial compensation of spontaneous electric polarization due to formation of heliconical structure.